ACS OMEGA

http://pubs.acs.org/journal/acsodf

Article

One-Pot Synthesis of Anatase, Rutile-Decorated Hydrogen Titanate Nanorods by Yttrium Doping for Solar H_2 Production

Sovann Khan, Hiroshi Ikari, Norihiro Suzuki, Kazuya Nakata, Chiaki Terashima, Akira Fujishima, Ken-ichi Katsumata,* and Vicente Rodríguez-González*

Cite This: *ACS Omega* 2020, 5, 23081−23089

Read Online

ABSTRACT: We have prepared yttrium (Y)-doped hydrogen titanate nanorods (HTN) by a microwave-assisted hydrothermal method. Y-doped HTN showed much improved photocatalytic activities for both H_2 evolution and dye decomposition. H_2 production from a methanol−water solution under UV−visible light for 7 h was enhanced by a factor of 5.5 with 1 wt % Y-doping. Doping with Y^{3+} ions reduced the band gap of HTN by ∼0.28 eV and induced new phases of anatase and rutile. High photocatalysis by Y-doping was attributed to enhanced light absorption (smaller band gap) and effective charge separation (heterojunction). To optimize H_2 production, a series of experiments examining effects of doping concentrations and non-noble surface metal (e.g., Ni, Cu, Co) loading were carefully performed. Y-doping in this work is a new and promising approach for synthesizing highly active HTN by producing the HTN/rutile/anatase heterostructure within the one-pot method.

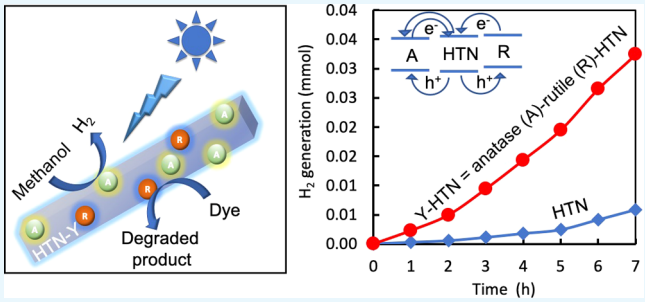

1. INTRODUCTION

Nanostructured titanates have shown their potentials in the development of functional materials for environmental and energy applications. Many titanate materials, $M_xTi_yO_{(x/2+2y)}\cdot zH_2O$ (M = H, Li, Na, K), have been successfully synthesized and are in common use as starting precursors for nanostructured titanium dioxide, TiO_2.[1−5] Titanate materials have layered structures composed of TiO_6 octahedral units packed together by sharing corners and edges, which leave voids between the layers. As a result, layered titanates have distinct properties such as large ion exchange capacity, fast ion diffusion and intercalation, and high surface charge density.[1] By controlling the structures of titanates, different nanostructures of TiO_2 were produced such as one-dimensional (1D) (tube, rod, wire, or belt), two-dimensional (2D) sheet, and hierarchical three-dimensional (3D) structures.[1,4] 1D structural materials exhibit unique functional properties for various applications including photocatalysis (e.g., pollutant degradation, CO_2 reduction, water splitting, and others),[6,7] electrocatalysis and batteries.[8,9] Among the titanate groups, hydrogen titanate nanotubes/rods (HTN), commonly found as $H_2Ti_3O_7$, $H_2Ti_4O_9\cdot H_2O$, $H_2Ti_2O_5\cdot H_2O$, and $H_{0.7}Ti_{1.825}\square_{0.175}O_4\cdot H_2O$ (□ = vacancy), are generally obtained by proton-exchange of alkali titanates and used as starting precursors for the synthesis of TiO_2 nanotubes by simple annealing.[10−14]

Instead of wasting energy for annealing to produce well-known TiO_2, HTN also has shown great promise for direct use as a photocatalytic material. Many attempts have been made to utilize HTN for effective photocatalytic reactions such as hydrogen evolution,[11] microbial deactivation,[12,13] and organic materials decomposition.[10,14] However, the photocatalytic activity of titanates was consistently lower than those of conventional catalysts of anatase, rutile, or heterostructured TiO_2−P25.[5,15] Titanates have a large band gap, which is only activated under ultraviolet (UV) light, resulting in low photocatalytic activity under a broad spectrum of solar light. Similar to other semiconductor photocatalysts, fast electron−hole pair recombination is a common barrier leading to low photocatalytic activities.

To overcome these issues, band gap engineering by doping was conventionally implemented to improve photocatalytic activities of large-band gap semiconductors by enhancing light absorption capability and charge separation.[16] In addition to doping, heterostructures of two or more materials were designed to improve photocatalytic reactions through a charge separation mechanism. Saito et al.[15] mixed P25 with titanate and used the composite as a photocatalyst for H_2 evolution from methanol aqueous solution and formic acid oxidation.

Received: June 15, 2020
Accepted: August 13, 2020
Published: August 31, 2020

https://dx.doi.org/10.1021/acsomega.0c02855
ACS Omega 2020, 5, 23081−23089

The composite of P25/titanate showed higher photocatalytic activities than the individual photocatalysts. Both excited electrons and holes were proposed to transfer from titanate to P25, which attributed to the electron−hole pair separation and enhanced photocatalytic activities. Later, a rutile/titanate heterojunction was reported as a high-performance photocatalyst for H_2 evolution from methanol aqueous solution. Since the conduction band positions of titanate and rutile are almost the same, excited electrons can transfer from titanate to rutile and vice versa. Additionally, holes were transferred from titanate to rutile, resulting in enhanced charge separation and photocatalytic activities.[5] Recent reports well demonstrated the charge-separation mechanism of anatase/rutile/titanate photocatalysts, which results in improved photocatalytic activities.[3−5,15]

Earth-abundant yttrium was successfully used as a dopant for improving the photocatalytic activity of TiO_2. It was reported that Y-doping slightly reduced the band gap of TiO_2 and facilitated the charge separation, resulting in higher photocatalytic activities.[17,18] A number of work has also been reported on the enhanced photocatalysis of TiO_2 by Y-codoping with other elements such as V−Y,[19,20] F−Y,[21] and B−Y.[22] However, the effect of Y-doping on HTN photocatalysis has not been reported yet. In this work, we proposed a new approach for synthesizing highly active HTN by introducing yttrium ions (Y^{3+}) during the hydrothermal step. We found that doping with Y^{3+} ions slightly reduced the band gap of HTN and induced secondary phases of rutile and anatase TiO_2. Photocatalytic H_2 evolution, photocurrent density, and eosin B dye degradation were much enhanced with Y-doping because of the improved light absorption (band gap reduction) and charge separation (heterojunction). Therefore, Y-doping should be an alternative method to improve titanate-based photocatalysts within one-pot process.

2. RESULTS AND DISCUSSION

Crystal phases of synthesized HTN with different Y-concentrations were identified by X-ray diffraction (XRD) analysis as plotted in Figure 1. The long-range XRD spectrum of undoped HTN shows a pure orthorhombic phase of $H_2Ti_2O_5{\cdot}H_2O$, which fits well with JCPDS #47-0124 (Figure 1a). The microwave-assisted hydrothermal method enabled the complete conversion of TiO_2 precursors to titanate species under strong alkali conditions. After proton exchange by HCl washing, HTN was formed.[1] Our previous studies[12] also obtained the same phase from this method. It was surprised that introducing the yttrium nitrate into the starting precursors produced secondary phases, which were identified as anatase (JCPDF #84-1286) and rutile TiO_2 (JCPDS #73-1232). The phase compositions were estimated by the proportion of area under the XRD curves at 9.4, 25.2, and 27.3° for planes (200) of HTN, (110) of anatase, and (101) of rutile, respectively. Doping of 1 wt % of Y promoted anatase and rutile formation by ∼46 and 5.7%. Upon increasing the Y-doping concentration to 3 wt %, the rutile phase was increased to 13.4 wt %, but the anatase phase decreased to 44.6 wt %. With a further increase of Y content to 5 wt %, both anatase and rutile decreased to 40.6 and 5.8 wt %, respectively.

To investigate the doping behavior of Y^{3+} ions, short-range XRD was plotted at 5−15 and 22−28° of pure HTN peaks and mixed peaks of HTN, anatase, and rutile (Figure 1b). These short-range XRD spectra show a small shift to lower angles with Y-doping, typically for the peaks for HTN and anatase.

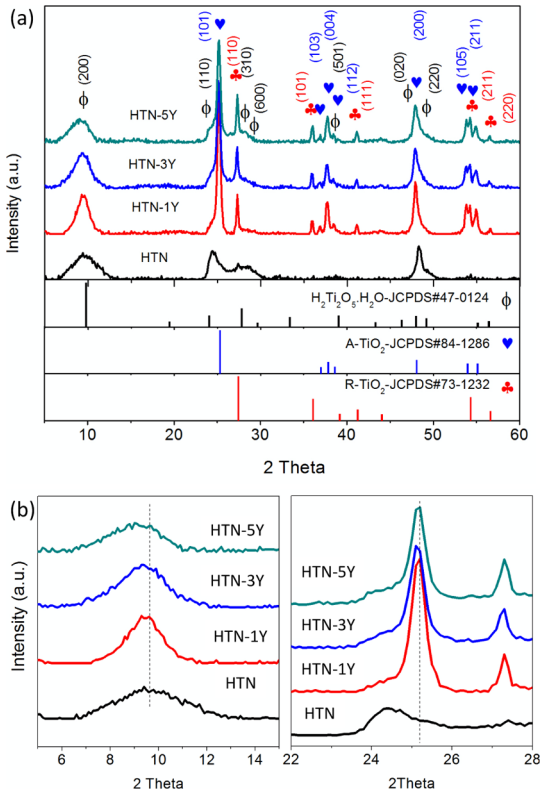

Figure 1. (a) Long-range XRD spectra and (b) short-range XRD spectra at 5−15 and 22−28° of HTN and x % Y-doped HTN (x = 0, 1, 3, 5 wt %).

The effective ionic radius of Y^{3+} ions (104 pm, VI coordination) is larger than that of Ti^{4+} ions (74.5 pm).[23] Therefore, incorporating Y^{3+} ions into HTN or TiO_2 leads to an extension of the lattices of the unit cells, resulting in the low-angle shift of XRD. To confirm the phase compositions and strained tubular structures, Raman shift analysis was used to identify the crystal structures of the materials, as shown in Figure 2. Broad peaks of undoped sample appeared at 278,

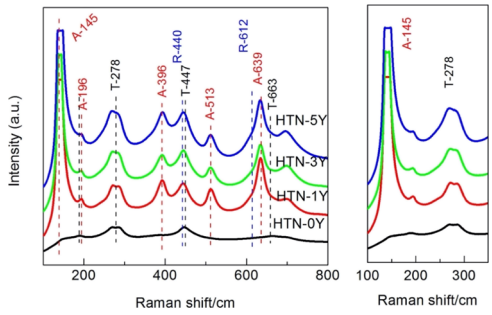

Figure 2. Raman shift of HTN and Y-doped HTN (Y = 0, 1, 3, 5 wt %) [A = anatase, R = rutile, T = HTN].

447, and 663 cm^{-1}, which are known as vibration peaks of titanate species.[11] Y-doping clearly results in new Raman peaks. Distinct peaks at 145, 196, 396, 513, and 639 cm^{-1} correspond to the anatase phase.[24] From XRD data, rutile was also included in the Y-doped HTN samples. The overlaps of Raman vibrational peaks of anatase, rutile and HTN produced broad peaks at 430−450 and 620−670 cm^{-1}. The broad peaks at 430−450 cm^{-1} should originate from rutile (E_g ∼ 440

https://dx.doi.org/10.1021/acsomega.0c02855
ACS Omega 2020, 5, 23081−23089

cm^{-1})[25] and HTN (447 cm^{-1}), while the peaks at 620−670 cm^{-1} should be from rutile (A_g ~ 612 cm^{-1}),[25] anatase (E_g ~ 639 cm^{-1}),[24] and HTN (663 cm^{-1}).[11] To confirm these compositions, home-made anatase, home-made rutile, and commercial P25 were also analyzed and Raman spectra are plotted in Supporting Information, Figure S1. In addition to the appearance of new peaks, doping with Y^{3+} ions induced a small shift to higher wavenumbers with the increase of doping concentrations, typically at 145 cm^{-1}. This shift confirmed the extension of the crystal lattice by the larger dopant of Y^{3+} ions.[24]

From XRD and Raman analysis, we conclude that some Y^{3+} ions were successfully doped into HTN crystal lattices. Nishimoto[26] and Byeon et al.[27] prepared $HLnTiO_4$ from proton exchange of $NaLnTiO_4$ (Ln = La, Nd, Sm, Gd, Y). They also observed that the change of lattice parameters were dependent on ionic sizes of Ln^{3+} ions.[26,27] In our cases, we doped only small amount of Y^{3+} (<5%), before proton exchange, the crystal phases of Y-doped and undoped samples were the same as $Na_2Ti_nO_{(2n+1)}$ parent phase (see XRD in Figure S2). Y^{3+} ion would be dopant and termed chemical composition as $Na_2Y_xTi_{(n-x)}O_{(2n+1)}$ (Scheme 1). During treating with HCl solution, Na^+ was exchanged by H^+ to form $H_2Y_xTi_{(2-x)}O_5{\cdot}H_2O$ lepidocrocite-type layered titanates.[28] However, anatase and rutile were also formed during proton exchange with Y-doped samples. Incorporation of different oxidative state (Y^{3+} vs Ti^{4+}) and large size of Y^{3+} ions might lead to induce defects (1)[28] and create strain (2) between octahedral TiO_6 layers,[26] which disturbs the recrystallization of titanate nanotubes to form anatase and rutile. Zhu et al.[29] prepared anatase and rutile TiO_2 from proton exchange of titanate nanotubes at concentrated HCl and diluted HCl, respectively. Anatase and titanate have similar structures with crystal lattices of octahedral sharing four edges and the zigzag ribbons. So, when hydrogen titanate dehydrated the large structure units of zigzag ribbons remained unchanged, and rearranged to form anatase (topotactic reaction).[29] Defects such as oxygen vacancies of Y-doped HTN would enhance the dehydration due to rich of −OH group via 2(−OH) → (−O−) + H_2O.[28] In contract to anatase formation, rutile formed from reconstruction of detached TiO_6 octahedral units. Zhu et al. found that in concentrated acid, titanate broke to small clusters of TiO_6 octahedral units and restacked to form rutiles.[29] Therefore, yttrium doping would enhance defect formation and detachment of TiO_6 octahedral units (strain effects) during acid treatment, which resulted in formation of both rutile and anatase. It is noticed that increasing Y-concentration enhanced the rutile formation but reduced the anatase. It means that increase Y-concentration breaks the TiO_6 octahedral units of HTN, and re-assembles to form rutile.

Scheme 1. Synthesis Process of Y-Doped HTN/Anatase/Rutile and Phase Evolution (Rod-Shaped is HTN, Light-Green and Red Spheres Are Rutile and Anatase)

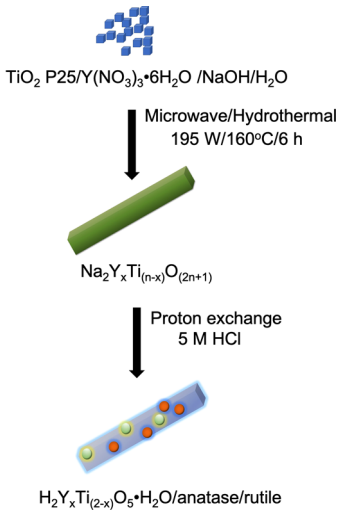

Further characterization by electronic microscopies will provide insights into the coexistence of anatase/rutile/hydrogen titanate and unrolling and ribbon-like structures due to the Y^{3+} cation incorporation. By scanning electron microscopy (SEM) observations shown in Figure 3, the HTN powder was composed of nanorod-like structures with non-uniform lengths and widths. In addition to rod-shaped particles, small particulates were also present. There was no significant differentiation of the particle structures with Y^{3+} ions observed by SEM. Further nanostructure investigation was performed by transmittance electron microscopy (TEM).

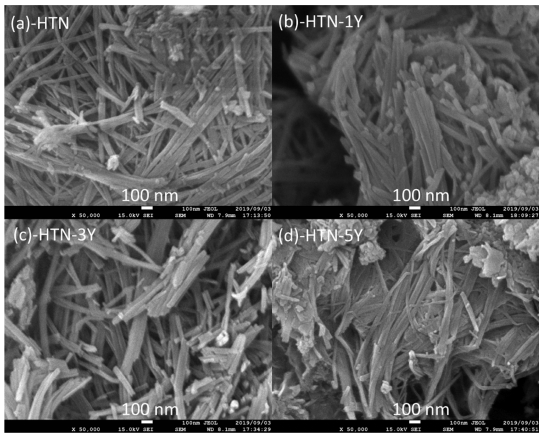

Figure 3. SEM images of HTN and Y-doped HTN (Y = 1, 3, 5 wt %) at 50k magnifications.

TEM images of HTN-1Y were taken randomly from several locations. General views of the particle structures at low magnification are shown in Figure 4a,b, with thin rod-shaped particles and a smaller number of particulates and nanosheets. High-resolution TEM images showed that the crystal phase of the rod-shaped particles was hydrogen titanate. The large lattice distance (~0.905 nm of average distance) was easily identified as the (200) plane of HTN (Figure 4c,d). More interestingly, on the surface of the HTN nanorods, there were small attached crystallites, identified as rutile and anatase phases based on lattice distances, which corresponded well to standard JCPDS data (Figure 4c,d).

We were curious about the phase of the particulate-structured particles seen in the SEM and low-magnified TEM images. Therefore, we analyzed the lattice distances of those particles and found that the majority was of the titanate phase, while a minority was anatase (data not shown). We analyzed 10 random images of the same sample, and few particles were identified as rutile. From the XRD data, 1 wt % Y^{3+} doping induced only 5.7% of rutile. Therefore, the rutile phase was hardly observed by TEM. From the microscopic studies, we found that the major structure of 1 wt % Y-doped

https://dx.doi.org/10.1021/acsomega.0c02855
ACS Omega 2020, 5, 23081−23089

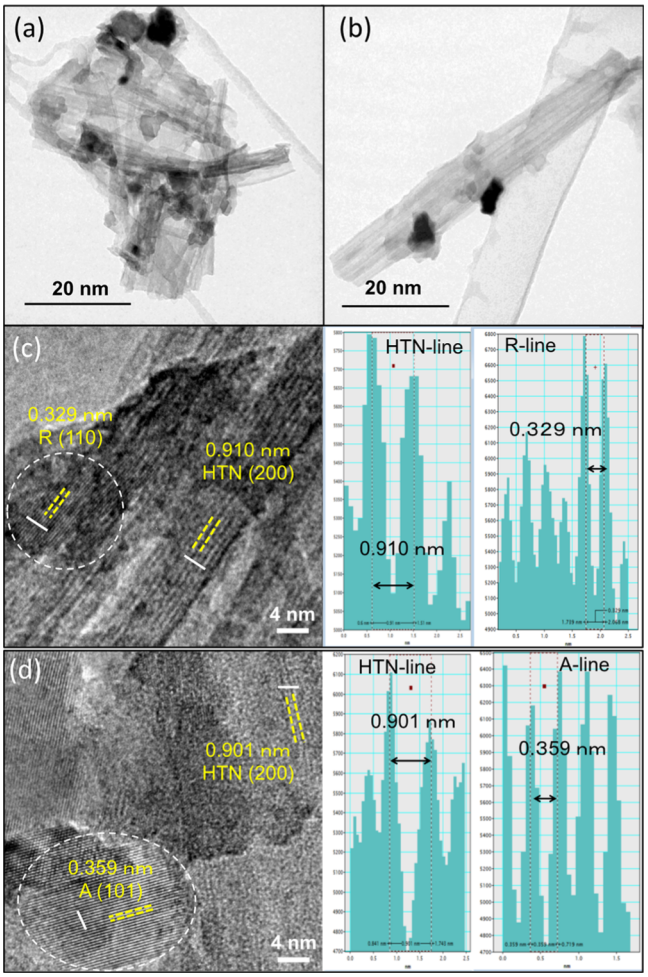

Figure 4. TEM images of HTN-1Y: (a) and (b) low-resolution images from two different locations; (c) HR-TEM image of rutile/HTN (left) and the corresponding line profiles of lattice fringes (right); (d) HR-TEM image of anatase/HTN (left) and the corresponding line profiles of lattice fringes (right).

HTN was composed of rod-shaped titanates decorated by small crystallites of anatase and rutile on the surface, while some nanotubes were open because of the strain.

Surface elemental states of HTN-1Y were examined by X-ray photoelectron spectroscopy (XPS) analysis and are plotted in Figure 5. Wide-range XPS spectra of HTN and HTN-1Y show clearly the identical compositions of Ti, O and C (Figure 5a).[10,13,14] A shallow peak at ∼158 eV, which was identified as Y 3d peak, was observed for HTN-1Y sample only when spectra were magnified at 150−170 eV (Figure 5a-inset). Deconvolution of high-resolution XPS spectra of all elements in HTN-1Y sample was plotted in Figure 5b. The Ti 2p XPS spectrum shows intense peaks at 459 and 465 eV, which are known to be $2p_{3/2}$ and $2p_{1/2}$ of the Ti^{4+} state of HTN. Co-existing peaks at 456.6 eV and 462 eV corresponded to $2p_{3/2}$ and $2p_{1/2}$ of the Ti^{3+} state of HTN.[2,13] O 1s peaks of HTN were deconvoluted into three peaks at 530, 531, and 533 eV, which were characterized as O species bound to the Ti^{4+} lattice (O−Ti^{4+}), oxygen bound to Ti^{3+} species, and surface hydroxyl groups, respectively.[2] Broad peaks at 156−162 eV were identified as binding energies of spin−orbit couplings of Y 3d ($3d_{5/2}$ and $3d_{3/2}$).[17,22] There were no Y 3d peaks detected in pure HTN (data not shown). These XPS data confirmed

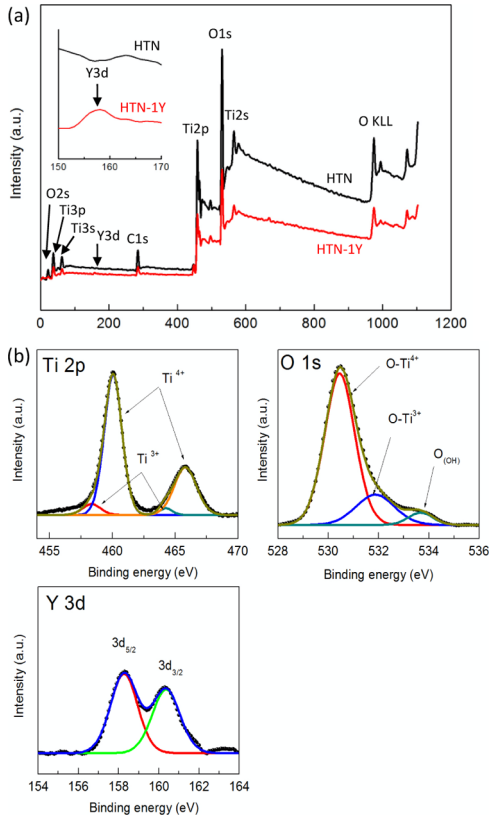

Figure 5. (a) Wide-range XPS spectra of HTN and HTN-1Y; (b) deconvoluting XPS spectra of Ti 2p, O 1s, and Y 3d of HTN-1Y (dots are experimental data and lines are fitting data).

that the Y^{3+} ions were doped into our samples. Y concentrations obtained from XPS data were 1.99, 5.54, and 7.05 at. % for HTN-1Y, HTN-3Y, and HTN-5Y, respectively, which were higher than the theoretical preparations.

UV−vis absorption spectra in Figure 6a show that undoped HTN absorbs light in the UV range (<380 nm). Doping with 1 wt % Y^{3+} ions slightly red-shifted the UV−vis absorption capabilities (>400 nm). The red-shift was not affected by further increasing the Y-doping contents to 3 and 5 wt %. The band gap energy calculated from the Tauc function[24,30] as indirect band gap materials was 3.28 eV for undoped HTN (Figure 6b). With all Y-doped samples, the band gap energy was reduced to ∼3.0 eV. This small reduction (∼0.28 eV) of band gap might be due to energy level formation inside HTN's band gap by Y-doping and the co-existence of smaller band gap anatase and rutile. Many studies on Y-doped/co-doped TiO_2 nanoparticles reported small band gap reductions with a small amount of Y^{3+} ion doping.[2,19,31,32] Based on density functional theory calculations, it was found that the Y-doping energy at Ti^{4+}-substitutional sites in TiO_2 was lower than that at O-sites.[17,19] Therefore, Y^{3+} ions preferentially occupied the Ti^{4+} sites in TiO_2. Y 3d states were induced at both the valence band and conduction band, which resulted in a small reduction of band gap and improved electron−hole pair separation.[17] Because Y^{3+} ions are bigger than Ti^{4+}, only a small amount (<1 at. %) was possibly doped into the crystal lattices.[17,32] There has been no such study for HTN materials. Since HTN has similar properties to TiO_2, we assume that the band gap reduction of HTN by Y-doping should originate from Y 3d state formations at both the conduction band and valence band. Increasing the Y^{3+} amount to 3 and 5 wt % did not

https://dx.doi.org/10.1021/acsomega.0c02855
ACS Omega 2020, 5, 23081−23089

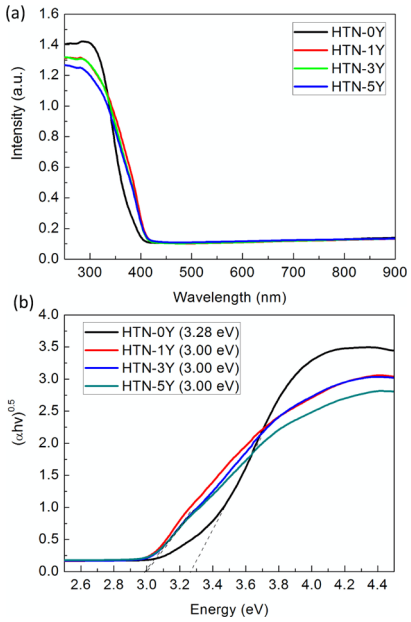

Figure 6. UV−vis absorption spectra (a) and optical band gaps from Tauc plots versus photon energy absorbed (b).

reduce the band gap any further. This was explained as a limitation of the doping concentration. Only a small amount of Y^{3+} ions were doped into the lattice, and the generation of heterostructured anatase/HTN/rutile aided the photocatalytic performance.

The effects of Y-doping on the photocatalytic activities of HTN were primarily evaluated by H_2 evolution reactions from a methanol−water mixture under UV−visible light (without UV cut-off filter). Figure 7a compares the H_2 amount produced by HTN and HTN-1Y. It was surprising that Y-doping significantly improved H_2 production. Within the 7 h reaction, H_2 production amounts from HTN and HTN-1Y were 5.9 and 32.4 μmol, respectively, an increase of a factor of 5.5 with the Y-doped sample. However, increasing the Y-doping contents to greater than 1 wt % did not show further improvement of the H_2 production rate as shown in Figure 7b. From the results, anatase phase played dominant role in enhanced photocatalytic activities of these composites. 1 wt % of Y-doping induced the highest fraction of anatase (∼46%). Therefore, 1-wt % Y-doped HTN was the optimized sample. Further photocatalytic activities of synthesized samples were evaluated by eosin B dye degradation and photocurrent measurements. Eosin B dye was very stable with undoped HTN photocatalysts. However, this dye solution degraded significantly with the Y-doped HTN photocatalyst (Figure 7c). Photocurrent densities obtained from HTN and HTN-1Y deposited on fluorine-doped tin oxide (FTO) glass were measured for 3 cycles for a total measurement time of up to 1500 s. Initial current densities were 16 and 67 $\mu A \cdot cm^{-2}$ for HTN and HTN-1Y, respectively. After 1500 s, current densities were reduced to 7 and 22 $\mu A \cdot cm^{-2}$ for HTN and HTN-1Y (Figure 7d). From the photocatalytic reaction experiments of H_2 generation, eosin B dye degradation and photocurrent measurements, we found that doping with Y^{3+} ions greatly improved the photocatalytic activities of HTN catalysts.

Next, the mechanism of enhanced photocatalytic activities by Y-doping was proposed as in Figure 8. From XRD, Raman and microscopic observations, we found that Y-doping induced secondary phases of anatase and rutile on the HTN particles. We believe that the most probable scenario existing in our samples is represented as an anatase/HTN/rutile heterostructure (see Figure 8a). Formed anatase and rutile nanoparticles are attached on the surface of HTN. Therefore, two separate heterostructures of anatase/HTN and rutile/HTN should mainly be formed. (1) Rutile/HTN: It was reported that the conduction band of rutile (CB_R) and

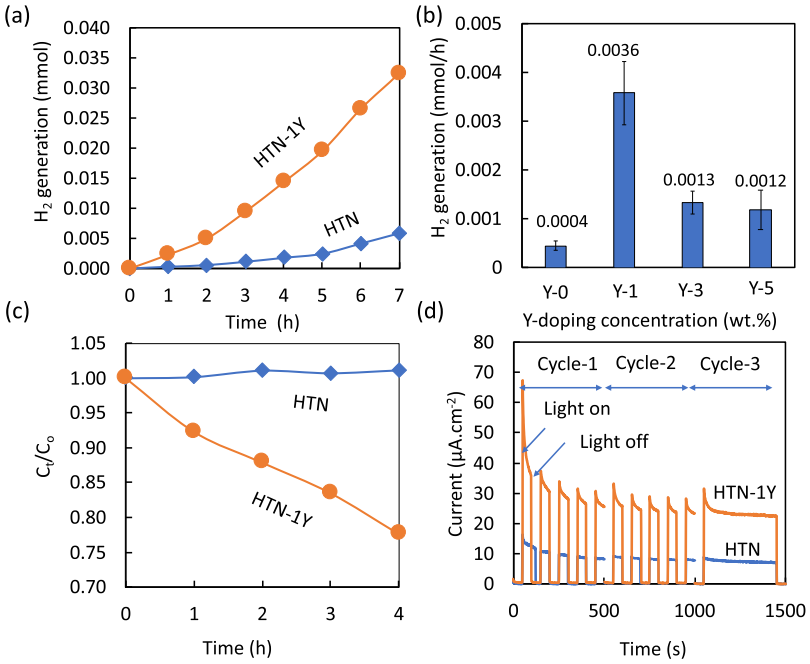

Figure 7. Photocatalytic activities: (a) H_2 generation from methanol−water mixture, (b) H_2 generation rates with different Y-doping contents (0, 1, 3, 5 wt %), (c) photodegradation of eosin B dye, and (d) photocurrent densities.

https://dx.doi.org/10.1021/acsomega.0c02855
ACS Omega 2020, 5, 23081−23089

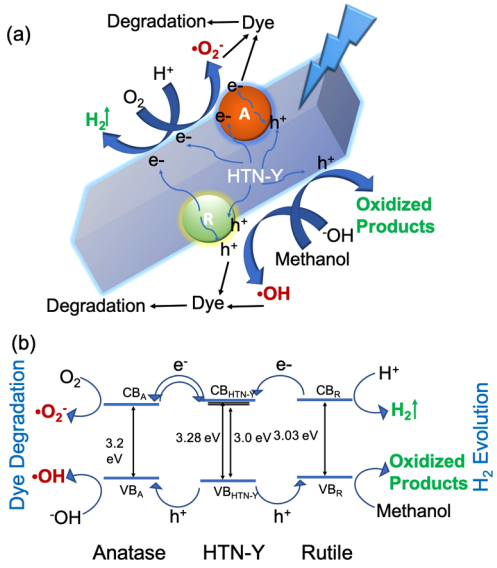

Figure 8. (a) Most probable scenario existing in our samples: anatase/rutile/HTN (rod-shape is HTN, light-green and red spheres are rutile and anatase); (b) band diagram of anatase/HTN and rutile/HTN heterostructures.

conduction band of titanate are almost identical (or, CB_R is 0.05 eV higher than titanate).[5] Considering the same situation in our case, the conduction band of HTN (CB_{HTN}) and CB_R are at the same energy level. Y-doping created a shallow energy level of the Y 3d state below CB_{HTN} (VB_{HTN}),[17] which reduced the band gap by 0.28 eV (see UV−vis absorption spectra) to 3.0 eV. Therefore, $CB_{HTN\text{-}Y}$ should be slightly lower than CB_R, which allows electrons transfer from CB_R to $CB_{HTN\text{-}Y}$ (Figure 8b-right). The approximated band gaps of rutile and anatase are 3.03 and 3.2 eV, respectively.[33] So, $VB_{HTN\text{-}Y}$ should be more positive than VB_R, which thermodynamically allows protons transfer from $VB_{HTN\text{-}Y}$ to VB_R. (2) Anatase/HTN: It is known that the conduction band of anatase (CB_A) is located 0.1 eV below the conduction band of titanate.[15,34] Y-doping might create energy levels below CB_{HTN} (formed $CB_{HTN\text{-}Y}$). Therefore, $CB_{HTN\text{-}Y}$ should be similar or slightly lower than CB_A, which allows electrons can transfer from CB_A to $CB_{HTN\text{-}Y}$ and vice versa. Ide et al. also proposed that electrons can transfer from anatase to titanate and also from titanate to anatase because of their similar conduction band location.[4] With its smaller band gap, VB_A is less positive than $VB_{HTN\text{-}Y}$. As result, holes thermodynamically flow from HTN-Y to anatase (Figure 8b-left).[11] In H_2 evolution reaction, holes at valence band of semiconductors react with methanol used as hole scavenger and produce protons and oxidized products (Figure 8b). Electrons at conduction band of composites react with H^+ to generate H_2 gas.[35] In organic dye degradation, electrons react with O_2 to form superoxide radicals ($^{\bullet}O_2^-$), which effectively degrade organic dyes such as eosin B. Holes at valence band react with hydroxyl group in water to form hydroxyl radicals ($^{\bullet}OH$), which further oxidize the dye molecules. Electrons and holes also react directly with dye to release oxidized or reduced products. Therefore, by these combined heterostructures, the enhanced photocatalytic activities in HTN-Y was attributed to the reduction in band gap, which enhances light absorption and effective charge separation by inducing anatase/rutile/HTN heterostructures.

To increase H_2 production, we also tried to load non-noble metals such as Cu, Ni, and Co by using *in situ* photoreduction methods. Loading metal nanoparticles on the HTN-Y did not change the phases of crystal structures (see XRD in Figure S3). No metal-related XRD peaks were observed either. This might be due to a very small amount of metal loading. UV−vis−NIR absorption spectra in Figure S4 show that shallow peaks at visible to NIR ranges appeared with metal nanoparticle loading. These are absorption characteristics of metal nanoparticles.[36] Photocatalytic H_2 generation of nickel loading on HTN and HTN-Y in Figure 9a shows that H_2 production by

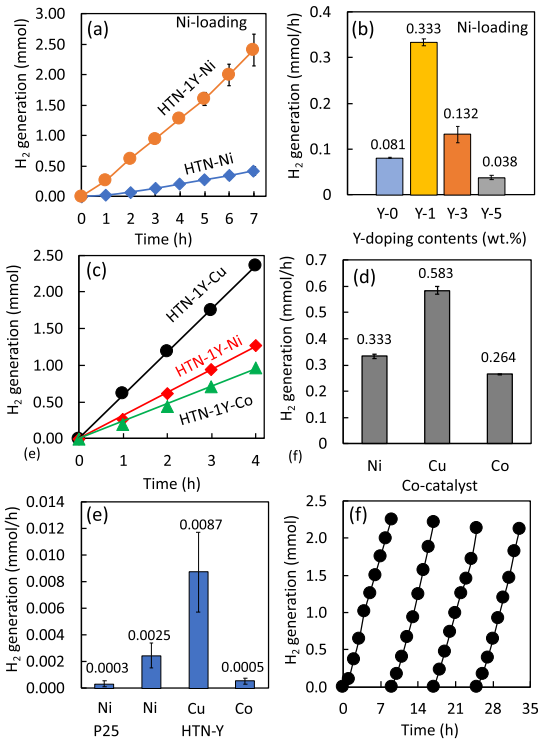

Figure 9. (a) H_2 production by HTN and HTN-1Y with 1 at. % of Ni loading under UV−visible light; (b) average H_2 production rates with different Y-doping concentrations at the same Ni-loading (1 at. %); (c) Comparing H_2 production by HTN-1Y loading with Cu (0.1%), Ni (1%), and Co (0.1%); (d) average H_2 production rates by HTN-1Y with metal-loading; (e) H_2 production rate under visible light with 400 nm-cut-off filter; and (f) recycling experiments for H_2 production from HTN-1Y with Ni-loading under UV−visible light.

Ni-loaded HTN-Y was much higher than Ni-loaded HTN. After 7 h of reaction, the total H_2 produced was 0.4 and 2.4 mmol from Ni-loaded HTN and Ni-loaded HTN-Y, respectively. The 1 wt % doped sample showed the highest H_2 production rate (Figure 9b). Therefore, 1 wt % of Y^{3+} is the optimum doping content for HTN in this work. Figure 9c shows H_2 production by HTN-1Y loaded with Cu, Ni, and Co. Concentrations of metal loading were prepared for 0.1 at.% for Cu and Co, and 1 at. % for Ni. These loading concentrations exhibited the highest H_2 generations from our optimization experiments (data not shown). The actual concentrations of metals obtained by XPS analysis were 1.45, 0.35, and 0.55 at. % for Ni, Cu and Co, respectively (see Figure S5). Average H_2 production rates were 0.583, 0.333, and 0.264 mmol/h for Cu, Ni, and Co loading, respectively (Figure 9d). This shows that Cu-loading afforded the best activities among these three metals. We compared photocatalytic H_2 evolution under UV−

https://dx.doi.org/10.1021/acsomega.0c02855
ACS Omega 2020, 5, 23081−23089

visible light using our samples with commercial P25. Unfortunately, P25 still worked better than our samples (see Table S1). However, it was interesting that when photocatalysis was performed under visible light (with UV cut-off filter, >400 nm), H_2 production by HTN-Y was higher than that of P25. Hydrogen production rates under visible light in Figure 9e show that Ni-loaded HTN-Y produced H_2 at 2.5 μmol/h, while Ni-loaded P25 produced only 0.3 μmol/h. Loading with Cu showed the best activity under visible light. Ide et al. also reported that from methanol aqueous solution under visible light, the titanate/anatase heterostructure showed higher photocatalytic H_2 production than that of P25 because the large band gap energy of P25 makes it highly active only under UV light.[4] Appearance quantum efficiency (QE) at 365 nm was calculated to be 2.25, 0.43 and 0.18% for HTN-Y loaded with Cu, Co, and Ni, respectively. The presence of multijunction of anatase, rutile, and Y-doped HTN enhances the photocatalytic performance under visible light in contrast with P25 that corresponds only to the anatase/rutile heterostructure which drives UV photocatalysis.

Finally, we examined the stability of the materials. We performed 4 cycles with HTN-1Y/Ni with a total radiation time of 35 h. The catalyst was washed with DI water after each cycle before the next use. More than 90% of H_2 production was maintained after 35 h of reaction (Figure 9f). The XRD profile of Ni-loaded HTN-Y after 35-h reaction was almost identical to that before the reaction (see Figure S6). This indicated that HTN was highly stable, and it would be a promising catalyst under UV light. The small reduction of H_2 generation was due to the loss of particles during the recycling procedure.

We compared the photocatalytic activities of our samples with related works published recently (see Table S1). We found that HTN-Y showed better photocatalytic H_2 production than other titanate catalysts (e.g., Ni-intercalated $Na_2Ti_2O_5{\cdot}nH_2O$,[11] $K_2Ti_4O_9$/anatase,[4] $K_xTi_{2-x/3}Li_{x/3}O_4$/anatase[3]). However, the photocatalytic activity of HTN-1Y under UV light was still less than that of commercial P25.

3. CONCLUSIONS

We successfully synthesized highly active HTN by Y^{3+} doping. Doping with Y^{3+} ions slightly reduced the band gap of HTN and induced new phases of anatase and rutile. This anatase/HTN/rutile heterostructure showed high photocatalytic activities for both H_2 evolution and dye degradation. Y^{3+} (1 wt %) exhibited the optimum doping content, which improved the H_2 production rate by ~5.5 times in the 7 h reaction. This large enhancement was attributed to enhanced light absorption (smaller band gap) and effective charge separation by the anatase/HTN/rutile heterostructure. To improve H_2 production, non-noble metals (e.g., Ni, Co, Cu) were loaded by an *in situ* photoreduction method. H_2 production rates under UV−visible light were increased from 0.0036 (HTN-1Y) to 0.583, 0.333, and 0.264 mmol/h by loading with Cu, Ni, and Co, respectively. Therefore, Y^{3+} doping would be a new approach for improving photocatalytic activities of HTN-based photocatalysts.

4. EXPERIMENTAL SECTIONS

4.1. Materials Synthesis. The synthesis of HTN was carried out by a microwave-assisted hydrothermal method, which was reported in our previous work.[12,13] 10 M NaOH (80 mL) and (x/274.92) M $Y(NO_3)_3{\cdot}6H_2O$ (10 mL) aqueous solutions were prepared separately by dissolving NaOH (J.T. Baker, ACS grade, USA) and $Y(NO_3)_3{\cdot}6H_2O$ (Sigma-Aldrich, USA) into distilled water and stirring for 10 min under ambient conditions. The amount of yttrium nitrate was calculated to yield 1, 3, and 5 wt % of yttrium with respect to TiO_2. The NaOH and yttrium nitrate solutions were poured into 150 mL Teflon tubes. Next, 2 g of dried TiO_2−P25 was slowly added into the above mixture, which was mixed by a magnetic stirrer for 10 min and sonicated for another 5 min. The precursor-containing Teflon tube was carefully sealed and placed into a microwave reactor (Eyela MWO-1000 Wave Magic microwave facilities, Japan). The reactor was heated by microwave irradiation at 160 °C for 6 h under 700 rpm magnetic stirring with a maximum variable microwave irradiation power of 195 W. The precipitated powders were cooled at room temperature and washed until neutralized to pH 7 with a 5 M HCl solution. The excess liquid was removed by vacuum system filtration using a microporous membrane (Pall, GH polypro, 0.2 μm). Finally, the solids were dried at 100 °C overnight. No further annealing was performed in this work.

4.2. Characterizations. Morphologies and nanostructures of the catalysts were studied by SEM (JSM-7699F, JEOL, Japan) and TEM (FEI Tecnai F30 microscope equipped with a tungsten field emission gun operated at 300 keV). Crystal structures were analyzed by XRD utilizing Cu Kα radiation at 1.5406 c5 (XRD, Ultima IV, Rigaku, Japan) with a scanning rate of 1°/min and Raman scattering spectroscopy (NRS-5100, Jasco, Japan). Optical properties were studied by UV−vis absorption spectroscopy (V-670, Jasco, Japan). Elemental compositions and surface areas were analyzed by XPS (ESCA-3400, Shimadzu, Japan) and gas absorption measurements (BELSORP-max, MicrotracBEL, Japan). Photocatalytic activities of the catalysts were evaluated by H_2 evolution from methanol aqueous solution under UV−visible light (mercury−xenon lamp, 300−1000 nm of wavelength, light intensity = 2.4 mW/cm^2 of UV 365 nm) and eosin B dye degradation. The catalyst (50 mg) was dispersed into 50 mL of deionized water by sonication for 20 min. In some cases, different moles of metal nitrates such as $Ni(NO_3)_2{\cdot}6H_2O$ (Sigma-Aldrich Inc., USA), $Cu(NO_3)_2{\cdot}3H_2O$ (Wako Chemical Corp., Japan), and $Co(NO_3){\cdot}6H_2O$ (Wako Chemicals Corp., Japan) were added to form metal-loaded catalysts.[37] The mixture was poured into a 300 mL glass cell covered with a quartz window, through which N_2 gas was bubbled for 30 min to remove oxygen contamination. After that, light was irradiated on the top of the cells. Gas (1 mL) was sampled every hour and injected into a gas chromatograph equipped with a thermal conductivity detector (TCD-GC, GC-2014, Shimadzu, Japan) for quantifying the gas composition. The apparent QE of hydrogen production was determined via the standard method.[38] Dye photodegradation evaluation was performed by the dispersion of 20 mg of catalyst into 20 mL of eosin B solution (0.018 mM) placed under UV light. After irradiation, the catalyst was removed by centrifugation at 13,000 rpm for 20 min. The remaining eosin B was quantified by UV−vis absorption spectroscopy.[39] Photocurrent densities of the catalyst films were measured by a VersaSTAT 4 system (METEK, USA) at a constant voltage of 0.8 V. Catalyst films were prepared by the dispersion of 20 mg of catalyst into 5 mL of ethanol by 10 min sonication and 30 min stirring. The mixture (3 mL) was dropped on the FTO glass and swiped by a doctor-blade to

https://dx.doi.org/10.1021/acsomega.0c02855
ACS Omega 2020, 5, 23081−23089

spread the catalyst on the FTO surface. Catalyst films were dried at 60 °C for 24 h before characterizations.

■ ASSOCIATED CONTENT

Supporting Information

The Supporting Information is available free of charge at https://pubs.acs.org/doi/10.1021/acsomega.0c02855.

Raman spectra, XPS, XRD data, UV, and table for comparison of previous works (PDF)

■ AUTHOR INFORMATION

Corresponding Authors

Ken-ichi Katsumata − *Photocatalysis International Research Center, Research Center for Space Colony, and Department of Materials Science and Technology, Faculty of Industrial Science and Technology, Tokyo University of Science, Noda-shi, Chiba 278-8510, Japan;* orcid.org/0000-0002-3841-5354; Email: k.katsumata@rs.tus.ac.jp

Vicente Rodríguez-González − *Photocatalysis International Research Center, Tokyo University of Science, Noda-shi, Chiba 278-8510, Japan; División de Materiales Avanzados, Instituto Potosino de Investigación Científica y Tecnológica (IPICYT), 78216, Mexico;* orcid.org/0000-0003-1145-174X; Email: vicente.rdz@ipicyt.edu.mx

Authors

Sovann Khan − *Photocatalysis International Research Center, Tokyo University of Science, Noda-shi, Chiba 278-8510, Japan;* orcid.org/0000-0003-0549-1841

Hiroshi Ikari − *Photocatalysis International Research Center, Tokyo University of Science, Noda-shi, Chiba 278-8510, Japan*

Norihiro Suzuki − *Photocatalysis International Research Center and Research Center for Space Colony, Tokyo University of Science, Noda-shi, Chiba 278-8510, Japan;* orcid.org/0000-0002-7154-3892

Kazuya Nakata − *Photocatalysis International Research Center, Tokyo University of Science, Noda-shi, Chiba 278-8510, Japan; Graduate School of Bio-Applications and Systems Engineering, Tokyo University of Agriculture and Technology, Koganei, Tokyo 184-0012, Japan*

Chiaki Terashima − *Photocatalysis International Research Center and Research Center for Space Colony, Tokyo University of Science, Noda-shi, Chiba 278-8510, Japan;* orcid.org/0000-0002-8874-1481

Akira Fujishima − *Photocatalysis International Research Center, Tokyo University of Science, Noda-shi, Chiba 278-8510, Japan*

Complete contact information is available at: https://pubs.acs.org/10.1021/acsomega.0c02855

Author Contributions

S.K. contributed for conceptualization, development of methodology, materials analysis, and writing-original-draft preparation. H.I. contributed for materials materials characterization. N.S., K.N., C.T., and A.F. contributed in support for materials characterizations and data interpretation. K.-i.K. and V.R.-G. contributed for funding acquisition conceptualization, supervision of experiments and writing-reviewing and editing.

Notes

The authors declare no competing financial interest.

■ ACKNOWLEDGMENTS

This research was financially supported by a Grant-in-Aid for JSPS Fellows (18F18337) from the Japan Society for the Promotion of Science (JSPS). S.K. received support from JSPS for his postdoctoral research (standard-P18337). V.R.-G. received support from CONACyT-Mexico for the Visiting Scientists and Scientists on Sabbatical Leave Fellowship Program 2018−2019. We thank Dr. Hector Silva-Pereira of LINAN-IPICYT for the HRTEM characterization of the materials studied in this work.

■ REFERENCES

(1) Zhang, Y.; Jiang, Z.; Huang, J.; Lim, L. Y.; Li, W.; Deng, J.; Gong, D.; Tang, Y.; Lai, Y.; Chen, Z. Titanate and titania nanostructured materials for environmental and energy applications: a review. *RSC Adv.* **2015**, *5*, 79479−79510.

(2) Lu, D.; Kumar Kondamareddy, K.; Fan, H.; Gao, B.; Wang, J.; Wang, J.; Hao, H. Highly improved visible-light-driven photocatalytic removal of Cr(VI) over yttrium doped H-Titanate nanosheets and its synergy with organic pollutant oxidation. *Sep. Purif. Technol.* **2019**, *210*, 775−785.

(3) Esmat, M.; Farghali, A. A.; El-Dek, S. I.; Khedr, M. H.; Yamauchi, Y.; Bando, Y.; Fukata, N.; Ide, Y. Conversion of a 2D lepidocrocite-type layered titanate into its 1D nanowire form with enhancement of cation exchange and photocatalytic performance. *Inorg. Chem.* **2019**, *58*, 7989−7996.

(4) Ide, Y.; Shirae, W.; Takei, T.; Mani, D.; Henzie, J. Merging cation exchange and photocatalytic charge separation efficiency in an anatase/$K_2Ti_4O_9$ nanobelt heterostructure for metal ions fixation. *Inorg. Chem.* **2018**, *57*, 6045−6050.

(5) Saito, K.; Tominaka, S.; Yoshihara, S.; Ohara, K.; Sugahara, Y.; Ide, Y. Room-temperature rutile TiO_2 nanoparticle formation on protonated layered titanate for high-performance heterojunction creation. *ACS Appl. Mater. Interfaces* **2017**, *9*, 24538−24544.

(6) Ge, M.; Cao, C.; Huang, J.; Li, S.; Chen, Z.; Zhang, K.-Q.; Al-Deyab, S. S.; Lai, Y. A review of one-dimensional TiO_2 nanostructured materials for environmental and energy applications. *J. Mater. Chem. A* **2016**, *4*, 6772−6801.

(7) Ge, M.; Cao, C.; Li, S.; Zhang, S.; Deng, S.; Huang, J.; Li, Q.; Zhang, K.; Al-Deyab, S. S.; Lai, Y. Enhanced photocatalytic performances of n-TiO_2 nanotubes by uniform creation of p−n heterojunctions with p-Bi_2O_3 quantum dots. *Nanoscale* **2015**, *7*, 11552−11560.

(8) Ge, M.; Tang, Y.; Malyi, O. I.; Zhang, Y.; Zhu, Z.; Lv, Z.; Ge, X.; Xia, H.; Huang, J.; Lai, Y.; Chen, X. Mechanically reinforced localized structure design to stabilize solid−electrolyte interface of the composited electrode of Si nanoparticles and TiO_2 nanotubes. *Small* **2020**, *16*, 2002094.

(9) Tang, Y.; Zhang, Y.; Malyi, O. I.; Bucher, N.; Xia, H.; Xi, S.; Zhu, Z.; Lv, Z.; Li, W.; Wei, J.; Srinivasan, M.; Borgna, A.; Antonietti, M.; Du, Y.; Chen, X. Identifying the origin and contribution of surface storage in TiO_2(B) nanotube electrode by in situ dynamic valence state monitoring. *Adv. Mater.* **2018**, *30*, 1802200.

(10) Rodríguez-González, V.; Obregón-Alfaro, S.; Lozano-Sánchez, L. M.; Lee, S.-W. Rapid microwave-assisted synthesis of one-demisional silver-$H_2Ti_3O_7$ nanotubes. *J. Mol. Catal. A: Chem.* **2012**, *353−354*, 163−170.

(11) Jang, J. S.; Choi, S. H.; Kim, D. H.; Jang, J. W.; Lee, K. S.; Lee, J. S. Enhanced photocatalytic hydrogen production from water−methanol solution by nickel intercalated into titanate nanotube. *J. Phys. Chem. C* **2009**, *113*, 8990−8996.

(12) Patrón-Soberano, A.; Núñez-Luna, B. P.; Casas-Flores, S.; De las Peñas, A.; Domínguez-Espíndola, R. B.; Rodríguez-González, V. Photo-assisted inactivation of Escherichia coli bacteria by silver functionalized titanate nanotubes, Ag/$H_2Ti_2O_5{\cdot}H_2O$. *Photochem. Photobiol. Sci.* **2017**, *16*, 854−860.

(13) Rodríguez-González, V.; Domínguez-Espíndola, R. B.; Casas-Flores, S.; Patrón-Soberano, O. A.; Camposeco-Solis, R.; Lee, S.-W. Antifungal nanocomposites inspired by titanate nanotubes for complete inactivation of Botrytis cinerea isolated from tomato infection. *ACS Appl. Mater. Interfaces* **2016**, *8*, 31625−31637.
(14) Rodríguez-González, V.; Ruiz-Gómez, M. A.; Torres-Martínez, L. M.; Zanella, R.; Gómez, R. Sol−gel silver hexatitanates as photocatalysts for the 4-chlorophenol decomposition. *Catal. Today* **2009**, *148*, 109−114.
(15) Saito, K.; Kozeni, M.; Sohmiya, M.; Komaguchi, K.; Ogawa, M.; Sugahara, S. Y.; Ide, Y. Unprecedentedly enhanced solar photocatalytic activity of a layered titanate simply integrated with TiO_2 nanoparticles. *Phys. Chem. Chem. Phys.* **2016**, *18*, 30920.
(16) Daghrir, R.; Drogui, P.; Robert, D. Modified TiO_2 for environmental photocatalytic applications: A review. *Ind. Eng. Chem. Res.* **2013**, *52*, 3581−3599.
(17) Khan, M.; Cao, W. Preparation of Y-doped TiO_2 by hydrothermal method and investigation of its visible light photocatalytic activity by the degradation of methylene blue. *J. Mol. Catal. A: Chem.* **2013**, *376*, 71−77.
(18) Kumar, K. S.; Song, C.-G.; Bak, G. M.; Heo, G.; Seong, M.-J.; Yoon, J.-W. Phase control of yttrium (Y)-doped TiO_2 nanofibers and intensive visible photoluminescence. *J. Alloys Compd.* **2014**, *617*, 683−687.
(19) Khan, M.; Cao, W. Cationic (V, Y)-codoped TiO_2 with enhanced visible light induced photocatalytic activity: A combined experimental and theoretical study. *J. Appl. Phys.* **2013**, *114*, 183514.
(20) Khan, M.; Li, J.; Cao, W.; Ullah, A. Advancement in the photocatalytic properties of TiO_2 by vanadium and yttrium codoping: Effect of impurity concentration on the photocatalytic activity. *Sep. Purif. Technol.* **2014**, *130*, 15−18.
(21) Zhang, H.; Miao, G.; Ma, X.; Wang, B.; Zheng, H. Enhancing the photocatalytic activity of nanocrystalline TiO_2 by co-doping with fluorine and yttrium. *Mater. Res. Bull.* **2014**, *55*, 26−32.
(22) Wu, Y.; Gong, Y.; Liu, J.; Zhang, Z.; Xu, Y.; Ren, H.; Li, C.; Niu, L. B and Y co-doped TiO_2 photocatalyst with enhanced photodegradation efficiency. *J. Alloys Compd.* **2017**, *695*, 1462−1469.
(23) Shannon, R. D. Revised effective ionic radii and systematic studies of interatomic distances in halides and chalcogenides. *Acta Crystallogr., Sect. A: Cryst. Phys., Diffr., Theor. Gen. Crystallogr.* **1976**, *32*, 751−767.
(24) Khan, S.; Cho, H.; Kim, D.; Han, S. S.; Lee, K. H.; Cho, S.-H.; Song, T.; Choi, H. Defect engineering toward strong photocatalysis of Nb-doped anatase TiO_2: Computational predictions and experimental verifications. *Appl. Catal., B* **2017**, *206*, 520−530.
(25) Mazza, T.; Barborini, E.; Piseri, P.; Milani, P.; Cattaneo, D.; Bassi, A. L.; Bottani, C. E.; Ducati, C. Raman spectroscopy characterization of Ti O_2 rutile nanocrystals. *Phys. Rev. B* **2007**, *75*, 045416.
(26) Nishimoto, S.; Matsuda, M.; Harjo, S.; Hoshikawa, A.; Kamiyama, T.; Ishigaki, T.; Miyake, M. Structural change in a series of protonated layered perovskite compounds, $HLnTiO_4$ (Ln= La, Nd and Y). *J. Solid State Chem.* **2006**, *179*, 1892−1897.
(27) Byeon, S.-H.; Yoon, J.-J.; Lee, S.-O. A new family of protonated oxides $HLnTiO_4$ (Ln = La, Nd, Sm, and Gd). *J. Solid State Chem.* **1996**, *127*, 119−122.
(28) Yuan, H.; Besselink, R.; Liao, Z.; Johan, E. The swelling transition of lepidocrocite-type protonated layered titanates into anatase under hydrothermal treatment. *Sci. Rep.* **2014**, *4*, 4584.
(29) Zhu, H. Y.; Lan, Y.; Gao, X. P.; Ringer, S. P.; Zheng, Z. F.; Song, D. Y.; Zhao, J. C. Phase transition between nanostructures of titanate and titanium dioxides via simple wet-chemical reactions. *J. Am. Chem. Soc.* **2005**, *127*, 6730−6736.
(30) Choi, H.; Khan, S.; Choi, J.; Dinh, D. T. T.; Lee, S. Y.; Paik, U.; Cho, S.-H.; Kim, S. Synergetic control of band gap and structural transformation for optimizing TiO_2 photocatalysts. *Appl. Catal., B* **2017**, *210*, 513−521.
(31) Plata, J. J.; Márquez, A. M.; Sanz, J. F.; Avellaneda, R. S.; Romero-Sarria, F.; Domínguez, M. I.; Centeno, M. A.; Odriozola, J. A. Gold nanoparticles on yttrium modified titania: Support properties and catalytic activity. *Top. Catal.* **2011**, *54*, 219−228.
(32) Zanella, R.; Rodríguez-González, V.; Arzola, Y.; Moreno-Rodriguez, A. Au/Y-TiO_2 catalyst: High activity and long-term stability in CO oxidation. *ACS Catal.* **2012**, *2*, 1−11.
(33) Scanlon, D. O.; Dunnill, C. W.; Buckeridge, J.; Shevlin, S. A.; Logsdail, A. J.; Woodley, S. M.; Catlow, C. R. A.; Powell, M. J.; Palgrave, R. G.; Parkin, I. P.; Watson, G. W.; Keal, T. W.; Sherwood, P.; Walsh, A.; Sokol, A. A. Band alignment of rutile and anatase TiO_2. *Nat. Mater.* **2013**, *12*, 798.
(34) Sakai, N.; Ebina, Y.; Takada, K.; Sasaki, T. Electronic band structure of titania semiconductor nanosheets revealed by electrochemical and photoelectrochemical studies. *J. Am. Chem. Soc.* **2004**, *126*, 5851−5858.
(35) Maeda, K. Z-scheme water splitting using two different semiconductor photocatalysts. *ACS Catal.* **2013**, *3*, 1486−1503.
(36) Yi, S.-S.; Zhang, X.-B.; Wulan, B.-R.; Yan, J.-M.; Jiang, Q. Non-noble metals applied to solar water splitting. *Energy Environ. Sci.* **2018**, *11*, 3128−3156.
(37) Khan, S.; Kubota, Y.; Lei, W.; Suzuki, N.; Nakata, K.; Terashima, C.; Matsushita, N.; Fujishima, A.; Katsumata, K.-i. One-pot synthesis of (anatase/bronze-type)-TiO_2/carbon dot polymorphic structures and their photocatalytic activity for H_2 generation. *Appl. Surf. Sci.* **2020**, *526*, 146650.
(38) Yu, J.; Ran, J. Facile preparation and enhanced photocatalytic H_2 production activity of $Cu(OH)_2$ cluster modified TiO_2. *Energy Environ. Sci.* **2011**, *4*, 1364−1371.
(39) Khan, S.; Han, J. S.; Lee, S. Y.; Cho, S.-H. ZnS nano-spheres formed by the aggregation of small crystallites and their photocatalytic degradation of eosin B. *Chin. J. Chem.* **2017**, *35*, 159−164.

https://dx.doi.org/10.1021/acsomega.0c02855
ACS Omega 2020, 5, 23081−23089